

FastPET: Near Real-Time PET Reconstruction from Histo-Images Using a Neural Network

William Whiteley, *Member, IEEE*, Vladimir Panin, *Member, IEEE*, Chuanyu Zhou, Jorge Cabello, *Member, IEEE*, Deepak Bharkhada, *Member, IEEE*, and Jens Gregor

Abstract—Direct reconstruction of positron emission tomography (PET) data using deep neural networks is a growing field of research. Initial results are promising, but often the networks are complex, memory utilization inefficient, produce relatively small image sizes (e.g. 128x128), and low count rate reconstructions are of varying quality. This paper proposes FastPET, a novel direct reconstruction convolutional neural network that is architecturally simple, memory space efficient, produces larger images (e.g. 440x440) and is capable of processing a wide range of count densities. FastPET operates on noisy and blurred histo-images reconstructing clinical-quality multi-slice image volumes 800x faster than ordered subsets expectation maximization (OSEM). Patient data studies show a higher contrast recovery value than for OSEM with equivalent variance and a higher overall signal-to-noise ratio with both cases due to FastPET's lower noise images. This work also explored the application to low dose PET imaging and found FastPET able to produce images comparable to normal dose with only 50% and 25% counts. We additionally explored the effect of reducing the anatomical region by training specific FastPET variants on brain and chest images and found narrowing the data distribution led to increased performance.

Index Terms—Positron Emission Tomography, Image Reconstruction, Neural Network, Deep Learning, Histo-Image.

I. INTRODUCTION

POSITRON emission tomography (PET) is a functional imaging modality utilizing biological tracers with wide ranging applications in oncology, cardiology, neurology and medical research. During a PET scan the distribution of a radioactive pharmaceutical administered to the patient is recovered through the process of image reconstruction. Typically, the data is relatively sparse and contains a high percentage of noise making this process a challenging inverse problem that is conventionally solved using either analytical or iterative reconstruction techniques. Analytical algorithms are fast and produce images that are quantitatively accurate, but suffer from low visual image quality with their characteristic streak artifacts. Iterative algorithms include well-studied statistical models in the reconstruction process and are more commonly used due to higher visual image quality. On the downside, these methods carry a higher computational burden requiring longer reconstruction times. More recently, a third category of reconstruction algorithms has emerged that utilize elements of machine learning and more specifically deep neural networks

in the reconstruction process. This category contains both hybrid techniques that combine a conventional method with machine learning and also direct reconstruction techniques where neural networks operate more or less directly on raw data to generate images. In this paper, we explore a novel technique in the direct neural network reconstruction category with the development of FastPET, a reconstruction method capable of producing clinical-quality multi-slice image volumes in near-real time. We analyze the computational cost as well as quantitative and qualitative aspects of image quality compared to the PET benchmark reconstruction algorithm known as Ordered Subsets Expectation Maximization plus Point Spread Function (OSEM+PSF) [1], [2]

Conventional reconstruction techniques solve the inverse imaging problem using either a closed form solution, as in the case of analytical methods, or an optimization algorithm, as in the case of iterative methods based on statistical models and corrections for noise such as scatter and randoms. This process stands in stark contrast to direct deep learning methods that learn all aspects of reconstruction using the data driven machine learning method of supervised learning. A concern often associated with these methods is the resulting trained network resembles a black box compared to the well understood and hand-crafted conventional algorithms. This trade-off must be weighed when considering the benefits of direct deep learning reconstruction methods.

FastPET and other direct neural network reconstruction methods offer benefits not found with traditional or even hybrid reconstruction techniques. Most immediate is the computational efficiency. While neural networks may take days or even weeks to learn a reconstruction model, a trained neural network can produce images in near real-time. This can improve workflow and remove reconstruction time as a consideration when developing PET scan protocols and selecting reconstruction parameters. Notable applications that would benefit therefrom include dynamic and gated studies that often include a large number of reconstructions as well as the development of interventional PET imaging techniques.

Beyond computational efficiency, data driven approaches are inherently flexible in their ability to learn an underlying model provided sufficient training examples and network capacity. The FastPET itself is a strong example of this by demonstrating a learned mapping from a very noisy input to a quality image. Creating the same mapping with hand-crafted features and algorithms would be a very long and difficult task. Given the ever increasing availability of more powerful computational resources combined with continued

W. Whiteley and J. Gregor are with the Department of Electrical Engineering and Computer Science, The University of Tennessee, Knoxville, TN, 37996 USA e-mail: william.whiteley@siemens-healthineers.com.

W. Whiteley, V. Panin, C. Zhou, J. Cabello, and D. Bharkhada are with Siemens Medical Solutions Inc. USA, Knoxville, TN 37932

Manuscript received Jan 30, 2020

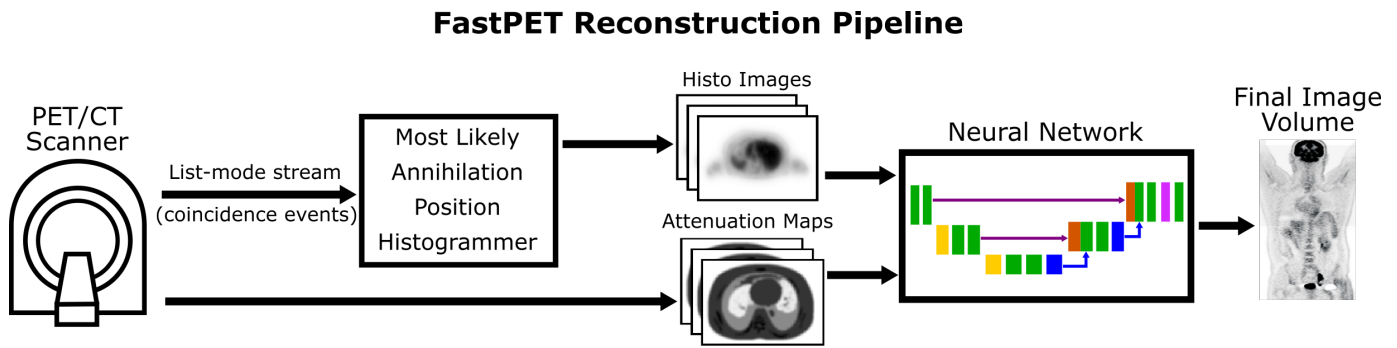


Fig. 1. FastPET consists of a most likely annihilation position histogrammer that places photon coincidences into a histo-image representation, and a convolutional neural network that uses attenuation maps to convert the histo-images into quantitative clinical-quality images.

improvements in deep learning methods, it is quite possible that learned reconstruction methods eventually will become common in medical imaging.

FastPET, as shown in Figure 1 and described in more detail in Section II, consists of a most likely annihilation position (MLAP) histogrammer, and a convolutional neural network. Raw coincidence events are converted to histo-images [3] which are fed to the neural network along with attenuation maps to create a quantitative clinical-quality image. This simple two-component approach takes advantage of the improved timing resolution of modern PET scanners, which has reduced the position uncertainty of annihilation events, combined with neural network research on denoising and deblurring.

Histo-images and their precursor histo-projections [4] have been studied since the development of time-of-flight (TOF) PET scanners [5]. A given histo-projection is a blurred version of the final image along the TOF dimension. However, modern scanners provide high resolution sampling in list-mode similar to image voxel size and when a regular image rectangular grid is utilized, the histo-projections become histo-images. The modern histo-image concept was introduced in the DIRECT framework [3] for fast reconstruction since histo-images are deconvolved into an image without any re-gridding allowing simultaneous reconstruction of many histo-images of various views.

The histo-projection approach typically exploits TOF data angular compression, such as transaxial mashing [6] and axial spanning [7] where adjacent angular histo-projections are combined. TOF angular compression results in relatively sparse angular sampling requiring TOF resolution to preserve spatial resolution [4], [6]. The DIRECT frame work used a similar compression tactic with histo-images and was able to achieve faster reconstructions but faced challenges with high sensitivity to data inconsistencies. While the single histo-image approach did not find a place in traditional reconstruction techniques, it has demonstrated potential in motion detection [8] and motion pre-correction [9], where a deblurring procedure may not be necessary.

Neural networks designed for deblurring and denoising is a frequent theme of deep learning research in general [10]–[13] and in medical imaging in particular. Neural network image space filters are often applied to improve images in low dose [14]–[16] or limited angle [17] X-ray computed tomography

(CT) applications, and in magnetic resonance imaging (MRI) to remove Rician noise [18] or reduce Gibbs artifacts [19]. These methods have been similarly applied in the PET low dose imaging domain to synthesize normal dose equivalents [20]–[23] utilizing U-Net [24] or ResNet [25] style networks. Jiao et al. [26] presented another neural network approach where images with the characteristic streak artifacts obtained from a simple inverse Radon transform were mitigated to the image quality standard of iterative reconstruction methods. The FastPET architecture capitalizes on some of this previous work to craft a neural network capable of deblurring the histo-images and correcting for noise such as attenuation, scatter, randoms and other noise sources in the photon detection process.

Despite the FastPET neural network operating entirely in image space, it has more in common with direct neural network reconstruction methods than with the image space filters discussed in the previous paragraph. FastPET operates on a histogrammed version of the raw PET data like other direct neural network reconstruction methods, but in this case the histogramming of coincidence events is into image space versus the typical process of histogramming events into a scanner’s geometrically defined sinogram space. This, in turn, requires the other neural networks to perform an expensive memory-space operation to transform the data into the image domain.

Generally speaking, direct reconstruction using neural networks in molecular imaging is not a new topic with active research dating back to at least the early 1990’s utilizing networks of fully connected multilayer perceptrons [27]–[30]. More recently, artificial intelligence has become an entirely new frontier for image reconstruction [31] capitalizing on two contributing factors: 1) the growth of computational resources, especially in graphical processing units (GPUs), multi-core central processing units (CPUs) and cloud computing; and 2) the development of better optimization algorithms and widely available deep learning software libraries such as PyTorch [32] and Tensorflow [33].

The AUTOMAP network [34] was the first direct reconstruction neural network to use modern deep learning techniques utilizing multiple fully connected layers followed by a sparse convolutional encoder-decoder to learn a mapping manifold directly from measurement to image space. AU-

TOMAP is capable of learning a general solution to the reconstruction inverse problem, but this generality is achieved by requiring an excessively high number of parameters limiting its application to relatively small single-slice images (e.g., 1x128x128). DirectPET [35] improved on this architecture for PET imaging by adding a convolutional encoder to compress the sinogram input along with a specially designed Radon inversion layer consisting of many small fully connected networks to more efficiently perform the domain transformation into image space. This allowed DirectPET to produce full size multi-slice image volumes (e.g., 16x400x400) directly from sinograms. DeepPET [36] developed by Häggström et al. is another example of direct neural network reconstruction but takes an alternative approach foregoing the memory intensive fully connected layers and instead, utilizing only convolutional layers to encode the sinogram input into a higher dimensional feature vector representation, which is then decoded by convolutional layers to produce a small single-slice image (e.g., 1x128x128). DeepPET produces smooth images with low noise, but fails at recovering detailed structures especially at low count densities where it often becomes unstable generating completely erroneous images.

As summarized in Table I, FastPET exhibits computational advantages compared with these other neural network approaches. Unlike AUTOMAP or DeepPET, which both produce small single slice images, FastPET is capable of producing multi-slice images that are comparable in size to those often used in clinical and research environments. Operating entirely on histo-images allows FastPET to utilize a relatively simple network architecture with orders of magnitude fewer network parameters than the other methods including DirectPET which also supports multi-slice reconstruction.

TABLE I
A COMPARISON OF MODERN DIRECT NEURAL NETWORK RECONSTRUCTION METHODS SHOWS THAT WHILE FASTPET IS CAPABLE OF FULL SIZE MULTI-SLICE RECONSTRUCTION, IT ALSO MAINTAINS A SIMPLE ARCHITECTURE WITH THE FEWEST PARAMETERS.

Method	Parameters	Network Complexity	Image size
AUTOMAP	1.34×10^9	Semi-complex	1x128x128
DirectPET	3.52×10^8	Complex	16x400x400
DeepPET	6.51×10^7	Simple	1x128x128
FastPET	3.24×10^6	Simple	8x440x440

II. FASTPET ARCHITECTURE

With reference to Figure 1, FastPET consists of two components, namely, a most likely annihilation position (MLPA) histogrammer that organizes the raw data into a histo-image representation, and a neural network that denoises and sharpens the histo-image. These two components are both computationally efficient and work well together to convert a stream of raw coincidence data into a clinical-quality multi-slice image volume in near real-time.

A. Most Likely Annihilation Position Histogrammer

The MLAP histogrammer provides fast approximate image generation capable of producing thousands of dynamic image

frames per second using standard computer hardware. The arrival time difference for two coincident events is used to estimate the most likely voxel along the line of response (LOR) where the annihilation event took place. Specifically, let the two detectors for the LOR be located at \vec{P}_1 and \vec{P}_2 and assume that the arrival time difference for the two photons is $\Delta t = t_1 - t_2$. The MLAP is then given by

$$\vec{P}_{\text{MLAP}} = \frac{\vec{P}_1 + \vec{P}_2}{2} + c \frac{\Delta t}{2} \frac{\vec{P}_1 - \vec{P}_2}{\|\vec{P}_1 - \vec{P}_2\|} \quad (1)$$

where c denotes the speed of light. The current MLAP histogrammer increments a counter for the nearest voxel, if the event was a prompt; conversely, the counter is decremented, if the event was a delay (random). Apart for randoms subtraction, no other physical corrections such as attenuation or scatter estimation, are involved in histo-image formation.

B. Neural Network Architecture

The FastPET neural network, shown in Figure 2, utilizes a U-NET [24] style architecture with the typical contracting, bottle neck and expanding segments where the number of convolutional kernels is doubled each time the spatial resolution is reduced and the number of convolutional kernels is halved each time the spatial resolution is increased. The proposed network also includes a standard residual block [25] at the end to provide additional refinement capability to the network. Overall, the network contains 17 convolutional layers (the ResNet block contains two convolutional layers) and has just over 3.24×10^6 learnable parameters. Each layer uses 3x3 convolutional kernels and a parametric rectified linear unit (PReLU) [37] activation functions. Spatial down-sampling is accomplished by using a kernel stride of 2, while up-sampling is accomplished using an efficient sub-pixel convolutional layer called PixelShuffle [38].

The neural network input is a series of n full size adjacent histo-images (i.e. $n \times 440 \times 440$) along with the corresponding attenuation maps generated from the scanner's x-ray CT functionality. In the majority of this work 8 histo-image slices were used creating an input of $16 \times 440 \times 440$ and an image volume output of $8 \times 440 \times 440$. The choice of input axial depth is an interesting hyper-parameter and alternate configurations including 4 and 16 slices were explored that both produced good results. Since the convolution kernel operates simultaneously on both the trans-axial and axial directions of the volume provided to the neural network, the depth selection primarily relates to how much of the volume should be jointly de-blurred and de-noised along the axial direction. Multiple adjacent slices are helpful in providing additional and highly-correlated information to the network, but increasing the axial depth too much introduces slices on each end of the input volume with less correlation.

C. Neural Network Training

The FastPET neural network was implemented with version 1.3 of the PyTorch [32] deep learning library and trained and tested on a Nvidia Titan RTX GPU. Training occurred over 1,500 epochs with each epoch having 1,600 samples drawn

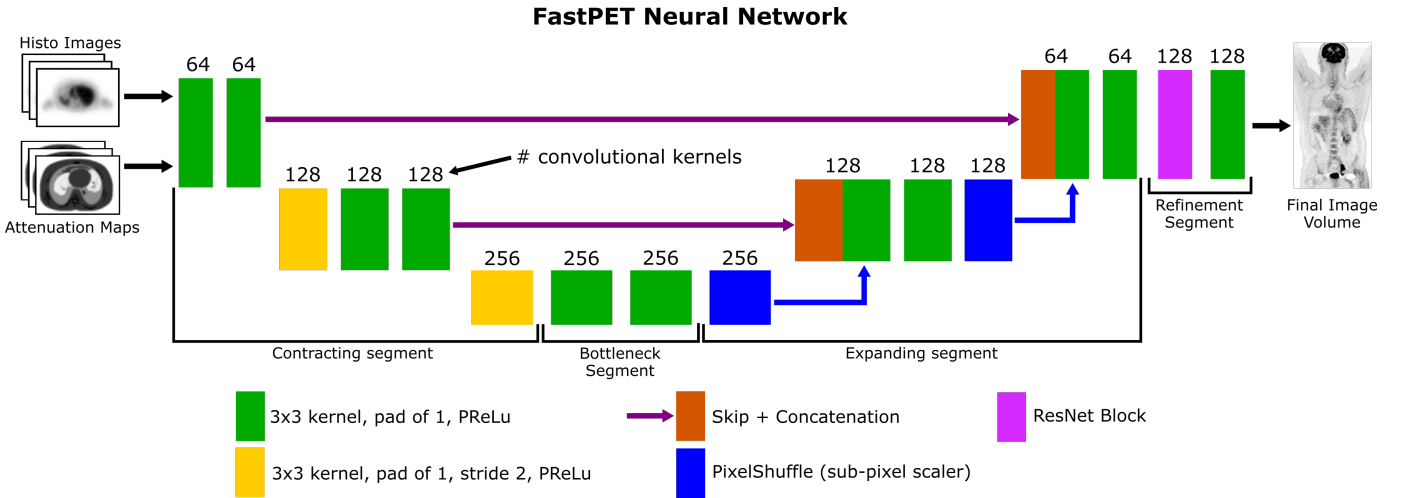


Fig. 2. The FastPET neural network utilizes a U-NET architecture followed by a single residual block creating a total of 17 convolutional layers. A kernel stride of 2 is used for down-sampling and PixelShuffle is used for up-sampling. All activation functions are parametric rectified linear units.

from the training data pool in mini-batches of 10. Each sample was set to contain a tuple of histo-image, attenuation map and target image, all with axial depth of 8. The Adam optimizer [39], which is similar to traditional stochastic gradient descent but additionally maintains a separate adaptive learning rate for each network parameter, was used with parameters $\beta_1 = 0.5$ and $\beta_2 = 0.999$. In addition to the optimizer, a cyclic learning rate scheduler [40] was employed to cycle the learning rate between experimentally determined lower upper bounds with the amplitude of the cycle decaying exponentially over time. This type of scheduler aids training since the periodic raising of the learning rate provides an opportunity for the network to escape sub-optimal local minimum and traverse saddle points more rapidly.

During training the optimizer minimizes the loss function through gradient descent updates. Zhao et al. published research [41] on loss functions for image generation and repair that suggested a weighted combination of an absolute measure, such as element-wise L1 loss like mean absolute error (MAE), and a perceptual measure, such as multi-scale structural similarity (MS-SSIM) [42], was optimal. The FastPet loss function trades-off these two elements using a dynamically balanced scale factor. An additional third loss term is added based on minimizing the difference of convolutional features extracted from the FastPET output and the training target using a VGG network [43]. The complete loss function used to minimize the difference between the proposed method's reconstructed image \hat{x} and a target image x was thus made to consist of three terms, specifically:

$$\mathcal{L}(\hat{x}, x) = \beta \text{VGG}(\hat{x}, x) + (1 - \alpha) \text{MAE}(\hat{x}, x) + \alpha \text{MS-SSIM}(\hat{x}, x) \quad (2)$$

The first loss component uses a VGG-16 neural network from the PyTorch library pre-trained for image classification on the large ImageNet data set. Each layer of the VGG-16 network is a feature extractor; earlier layers containing the smallest receptive fields extract fine image details, while deeper layers working on down-sampled images having larger

receptive fields extract broader semantic features. In our application, the output from the FastPET network and the target image are independently input to the VGG-16 network and features are extracted from the 1st, 4th, 7th, and 11th layers and the L1 loss between the two sets of features is added to the overall loss function.

The mean absolute error (MAE) denotes the common L1 pixel loss between reconstructed image \hat{x} and target image x calculated over all voxels, and the MS-SSIM term uses the standard formulation of structural similarity [42] over 5 image scales with a window size of 11×11 .

With respect to the weighting of the VGG loss, we used $\beta = 0.1$ for all updates and a dynamically calculated value for α that trades off the MAE and MS-SSIM losses against one another. That is:

$$\alpha = \frac{\sum_{j=i}^{i+n-1} \text{MAE}_j}{\sum_{j=i}^{i+n-1} \text{MAE}_j + \sum_{j=i}^{i+n-1} \text{MS-SSIM}_j} \quad (3)$$

where i and j are iteration steps and n denotes the width of a running average window.

D. Near Real-Time PET Imaging

A practical implementation of the FastPET architecture, as shown in Figure 3, is capable of generating multi-slice PET images from raw data with minimal delay. The raw list-mode data streaming from the PET/CT scanner is written to a memory mapped file that acts as a first-in-first-out (FIFO) buffer. The FastPET histogrammer continually processes the incoming list-mode data in an infinite loop writing the events to one of the memory mapped histo-image files in a pre-allocated circular buffer. The FastPET neural network also operates in a continuous loop summing the circular buffer's contents and performing a forward pass of the network with the summed histo-image and associated attenuation maps to generate a near real-time image.

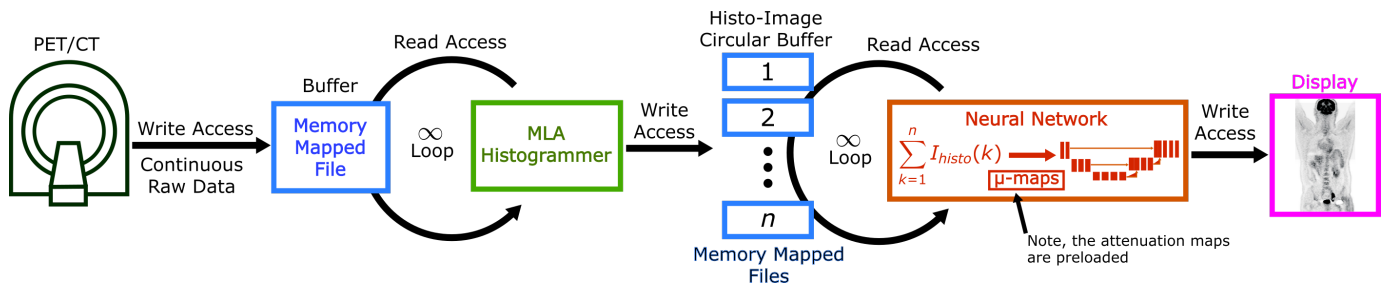


Fig. 3. A near real-time PET imaging pipeline showing an efficient architecture from the collection of raw events to the display in a user interface.

Two parameters must be selected in the proposed architecture, namely, the frame duration f in seconds, and the duration d also in seconds to aggregate and display in the real-time image viewer. The number of histo-images n in the circular buffer is then calculated as $n = (d/f) + 1$ and the FastPET histogrammer and neural network are in turn able to select the current histo-image in the circular buffer at time t as $h_k(t) = \lfloor t/f \rfloor \bmod n$. While the histogrammer is writing new events to the current histo-image, the neural network is reading and summing the previous $n - 1$ histo-images and generating a near real-time image.

When the target application is to view a continually growing image, which might be of interest when monitoring the progress of a PET scan in real-time, setting the aggregation duration to zero ($d=0$) results in the creation of a single histo-image in the circular buffer containing all annihilation events collected so far and skipping the summation step.

III. RECONSTRUCTION SPEED

The simplicity of the MLAP histogrammer combined with the computational efficiency of the neural network provides the most significant advantage of FastPET: reconstruction speed. A comparison of reconstruction speed between FastPET and the conventional reconstruction methods of Filtered Back-Projection (FBP) and OSEM+PSF both with TOF is shown in Figure 4. The conventional methods start from an uncompressed sinogram while FastPET starts from a histo-image. These two starting points are roughly computationally equivalent since both cases have the raw coincidence events histogrammed into a data structure appropriate for the method. The timing shown in the figure is to reconstruct a single 159 slice field-of-view (FOV) from the Biograph Vision PET/CT scanner [44]. The conventional reconstructions were performed on a HP Z8G4 computer containing an Intel Xeon Gold 6154 CPU running at 3.00 GHz. While 36 CPU cores are available on this system, the reconstruction was restricted to 12 by Siemens factory settings. The iterative OSEM+PSF reconstruction utilized 3 iterations and 5 subsets, and both iterative and analytical methods included attenuation and scatter correction as well as post-reconstruction smoothing. FastPET reconstructions were performed on an HP z840 computer with 2 Intel E5-2630 CPUs each with 10 cores running at 2.2 GHz and a single Nvidia Titan RTX GPU.

The results demonstrate the efficiency of neural network reconstruction with FastPET taking an average of 0.057 seconds

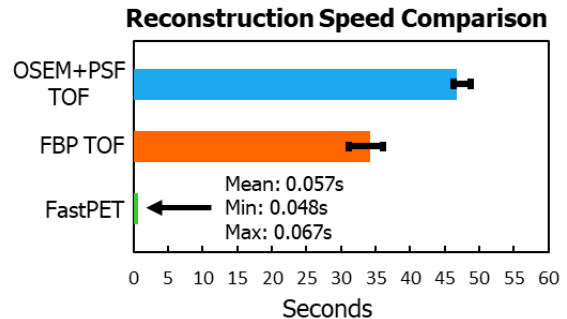


Fig. 4. A comparison between the reconstruction speed of conventional methods and FastPET for a single field-of-view for the Biograph Vision PET/CT shows that FastPET is about 820 times faster than OSEM and 600 times faster than FBP.

and 13.4 GB of GPU memory to reconstruct a 159x440x440 field-of-view by performing 2 forward passes of the neural network using an axial depth of 8 and a batch size of 10. By comparison OSEM+PSF reconstruction with TOF took an average of 46.73 seconds, while the same reconstruction averaged 34.16 seconds with the FBP algorithm also with TOF data. While this may not significantly affect the clinical workflow when a single static scan is considered, protocols that require many reconstructions would benefit from FastPET. In cardiology scans for example, the study of perfusion often requires around 10 gated reconstructions and the study of blood flow often requires around 26 dynamic frames. In these scenarios FastPET would complete these reconstructions in around 0.6 seconds and 1.5 seconds compared to about 8 and 20 minutes for the OSEM+PSF method. Additionally, the potential for entirely new reconstruction applications are enabled by ultra fast reconstruction such as interventional procedures, improved motion correction, or a near real-time PET image viewer.

IV. FASTPET IMAGE QUALITY ANALYSIS

A. Training and Validation Data

The primary data set used to develop FastPET was acquired on a Siemens Biograph Vision 8 ring PET/CT scanner [44]. This data set contains 55 raw list-mode wholebody patient studies acquired with a continuous bed motion protocol using the common PET fluorodeoxyglucose (^{18}F FDG) tracer, and including an X-ray CT scan for attenuation correction. This wholebody data set was split into 43 patients for training,

4 patients for validation used to tune the neural networks, and 8 patients for final model evaluation. The target images were created by reconstructing the data using the scanner's factory OSEM+PSF TOF protocol with a 440×440 image matrix, attenuation correction, scatter correction, a 5×5 mm post reconstruction Gaussian filter and all the standard included corrections (e.g. randoms smoothing, arc correction, etc.). To increase the training data and add additional variation, each of the patients in the training set was processed through 15 iterations of an augmentation protocol consisting of a random transaxial rotation between -60 and 60 degrees, a random translation of up to 30 pixels along both transaxial axes, and a random horizontal and vertical flip. This augmentation combined with the un-augmented data produced a total of 410,865 image slices in the training set.

Since image quality improvement of low dose PET images is a frequent topic of medical deep learning research, two low count data sets were derived from the original wholebody data set to explore this topic. The first data set had 50% of the counts removed randomly from the list-mode file, and the second data set had 75% of the counts removed.

Since the distribution of all possible wholebody images is a very large space, two additional data sets were used to explore the potential performance improvements of narrowing the data distribution. The first data set was again derived from the original wholebody data, but only contains the chest region starting from the top of the lungs and extending to the bottom of the liver resulting in 90,630 slices for training. A final data set acquired on the same PET/CT scanner consisted of 36 neurology brain scans split into 29 training, 3 validation and 4 test patients. Each of the scans is a single field-of-view with either a 300, 600 or 900 second duration. Preparation of this data utilized the same augmentation and conventional reconstruction parameters as the wholebody data, except the brain data set did not utilize a post-reconstruction filter. The result was 76,320 total slices for training the neural network.

B. Image Analysis

Three neural networks were trained from scratch on the original full-count wholebody PET data set with their convergence during training shown in Figure 5. The first network was provided the raw un-normalized histo-image but no attenuation maps, thus having a designation of FastPET-Raw-NAC (non-attenuation corrected). The second network was also provided the same un-normalized histo-image as well as the associated attenuation maps and given a designation of FastPET-Raw-AC. The third network, termed FastPET, was trained with histo-images normalized with PET crystal calibration parameters along with attenuation maps. Figure 5 clearly indicates the inclusion of attenuation maps leads to a significant improvement over using just the histo-images. One would expect inclusion of scanner normalization to result in marginally better results, but this does not significantly manifest itself in the plots shown here. However, since the normalization has negligible computational cost and in theory should provide a slightly better result, the base FastPET network and all derived networks utilize normalized histo-images.

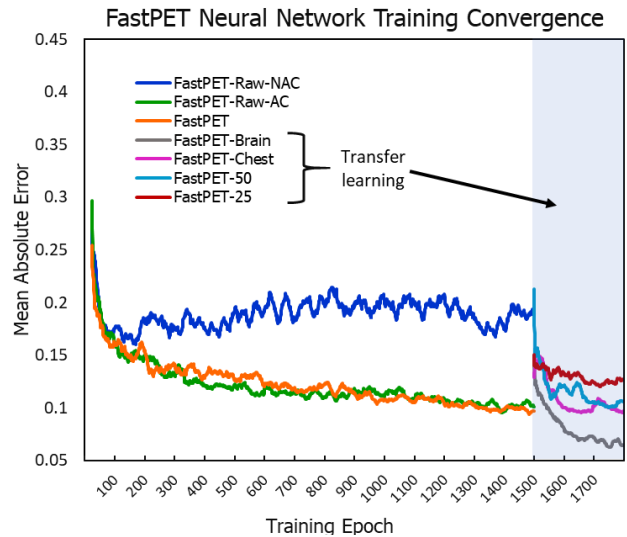


Fig. 5. Three FastPET neural networks were trained from scratch testing the affect of including attenuation maps and normalizing the histo-images. Four additional networks were subsequently trained using transfer learning to examine low dose compensation and narrow focus applications.

Four additional neural networks were trained to study the effect of varying the PET data distribution. However, since training each neural network from scratch took approximately 12 days on available hardware, these neural networks were trained using transfer learning. As a reminder, this is a process of fine-tuning a pre-trained neural network for a particular task by performing additional training on a task specific data set. The base neural network in this case was the best performing network (FastPET) trained from scratch on wholebody data. To explore low dose applications, two networks were trained on wholebody data that was decimated to contain respectively 50% of the data (FastPET-50) and 25% of the data (FastPET-25) with the target images still based on full count data. The impact of reducing the volume of the learned PET distribution, by narrowing the anatomical region considered, was also explored. The FastPET-Brain network was trained on a neurology data set and FastPET-Chest was trained on chest only images from the wholebody data set.

The derived networks were trained for an additional 300 epochs on their specific data set in the transfer learning phase. The convergence trends in Figure 5 seem to indicate that FastPET-Brain should perform especially well, while FastPET-Chest, which is also trained specifically for an anatomical region, only achieves loss comparable to the original network during training. In the low dose category, FastPET-50 achieves loss comparable to the network trained on the original data, which is promising, but FastPET-25 does not quite achieve the same level of performance. A summary of the trained networks is shown in Table II with their specified names to help distinguish between network results in the rest of this section.

C. Quantitative Image Performance

While it is critical to produce images that a radiologist can read visually, the quantitative measurement aspect of PET

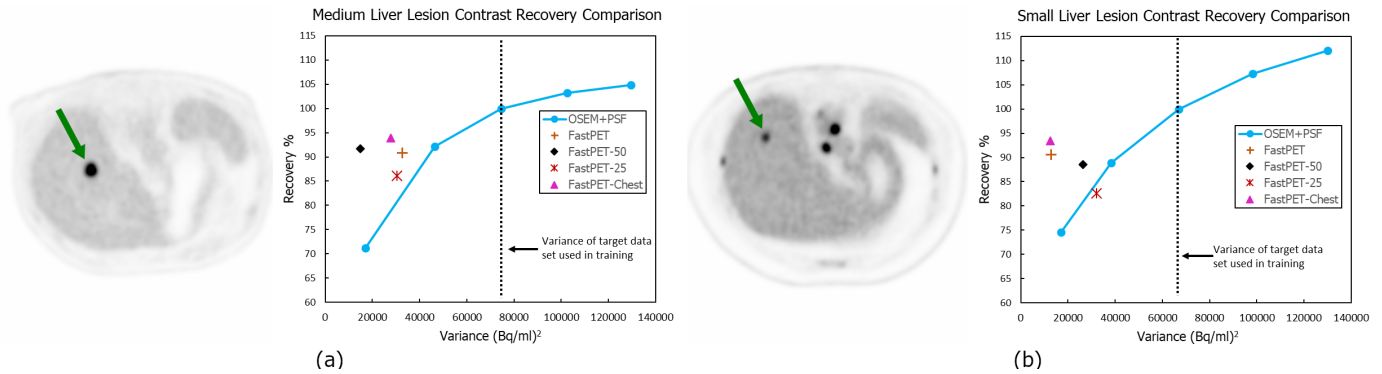


Fig. 6. The contrast recovery percentages of FastPET, its low count variants, and chest specific network are shown for two different liver lesions. The variance was calculated from ROIs in the liver and the lesion reference value is taken from the OSEM+PSF TOF reconstruction with 3 iterations, which is the same reconstruction used to train the neural networks.

TABLE II

MULTIPLE FASTPET NETWORKS WERE TRAINED, THREE FROM SCRATCH TO DETERMINE THE APPROPRIATE NETWORK INPUTS AND FOUR MORE THROUGH THE PROCESS OF TRANSFER LEARNING TO EXPLORE LOW DOSE AND ANATOMICALLY SPECIFIC VARIANTS OF FASTPET.

Network	Input	Data	Train Method
FastPET-Raw-NAC	Histo	WB 100%	from scratch
FastPET-Raw-AC	Histo+AC	WB 100%	from scratch
FastPET	Histo+Norm+AC	WB 100%	from scratch
FastPET-50	Histo+Norm+AC	WB 50%	transfer
FastPET-25	Histo+Norm+AC	WB 25%	transfer
FastPET-Brain	Histo+Norm+AC	FDG Neuro	transfer
FastPET-Chest	Histo+Norm+AC	WB Chest	transfer

imaging is becoming increasingly important in diagnosing and staging disease. With that in mind, using patient data FastPET was evaluated on the quantitative aspects of contrast recovery, noise levels and bias compared to conventional OSEM+PSF TOF reconstructions.

Figure 6 shows the results from two experiments comparing the contrast recovery of FastPET to OSEM+PSF. This measure shows the trade-off between variance/noise and the recovered tracer signal. In conventional iterative reconstruction a multi-point plot is created where the ratio of tracer recovered calculated from the mean value of the image voxels in a lesion are plotted against the variance in the image. However, for a patient scan the ground truth tracer activity of the lesion is unknowable, so the OSEM+PSF reconstruction with 3 iterations is the designated reference since it is also the number of iterations used to create the target images for neural network training. The variance is measured in a region of interest (ROI) in a relatively uniform area of the liver. The OSEM+PSF plot for each lesion is shown in the figure over five iterations with a light blue line. Note how in both lesion cases the third iteration has a recovery percentage of 100% since it is the designated reference.

Since the FastPET method does not have a tune-able variance parameter, a single point is plotted in each case for FastPET, namely, the two low count variants and the chest specific network. With reference to Figure 6a, which shows the results from the medium sized liver lesion, the neural network achieves greater tracer recovery for a given level

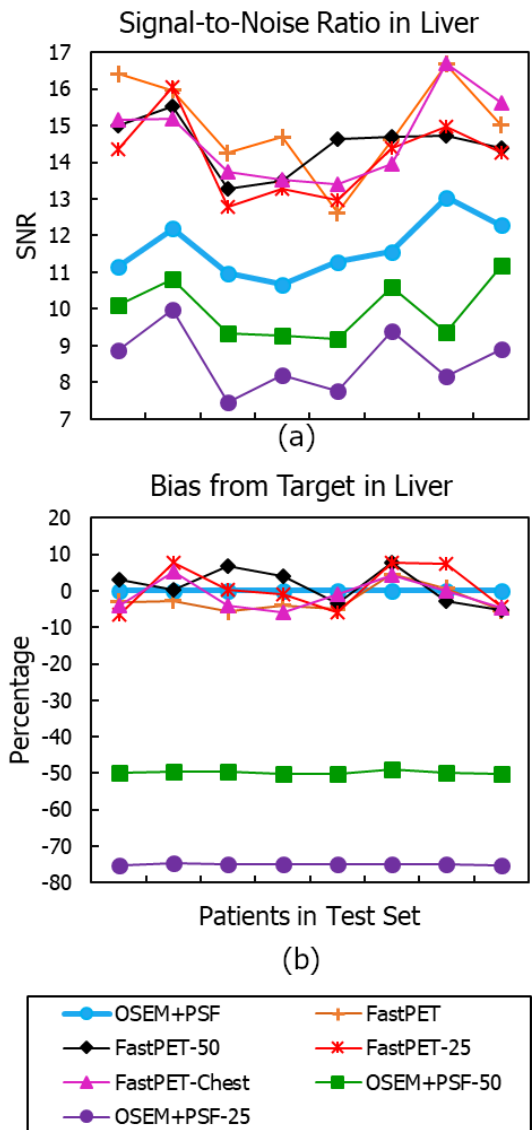


Fig. 7. Evaluations of signal-to-noise ratio and bias were conducted across all 8 patients of the test set. The SNR for the neural network reconstructions was consistently higher than OSEM+PSF TOF owing that outcome to the lower noise images. The bias measurements indicated non-systematic random bias variations across the test data set.

TABLE III

THIS TABLE CONTAINS QUALITATIVE PERFORMANCE MEASURED WITH MULTI-SCALE STRUCTURAL SIMILARITY FOR THE ENTIRE 3D IMAGE VOLUME. THE RESULTS INDICATE A HIGH PERCEPTUAL SIMILARITY BETWEEN FASTPET AND THE TARGET IMAGES EVEN WHEN THE NUMBER OF RAW COUNTS IS DECREASED. THE SAME CONSISTENCY IS NOT PRESENT IN TRADITIONAL RECONSTRUCTIONS GENERATED WITH THE SAME REDUCED COUNTS.

Validation Data	Raw Histo	FastPET	FastPET-50	FastPET-25	OSEM+PSF-50	OSEM+PSF-25
Patient 1	0.561	0.985	0.982	0.982	0.875	0.696
Patient 2	0.559	0.991	0.990	0.990	0.878	0.705
Patient 3	0.562	0.984	0.986	0.983	0.879	0.703
Patient 4	0.568	0.986	0.982	0.975	0.873	0.694
Patient 5	0.569	0.989	0.988	0.986	0.875	0.699
Patient 6	0.541	0.984	0.980	0.976	0.878	0.707
Patient 7	0.566	0.991	0.991	0.984	0.874	0.700
Patient 8	0.562	0.989	0.988	0.979	0.878	0.704

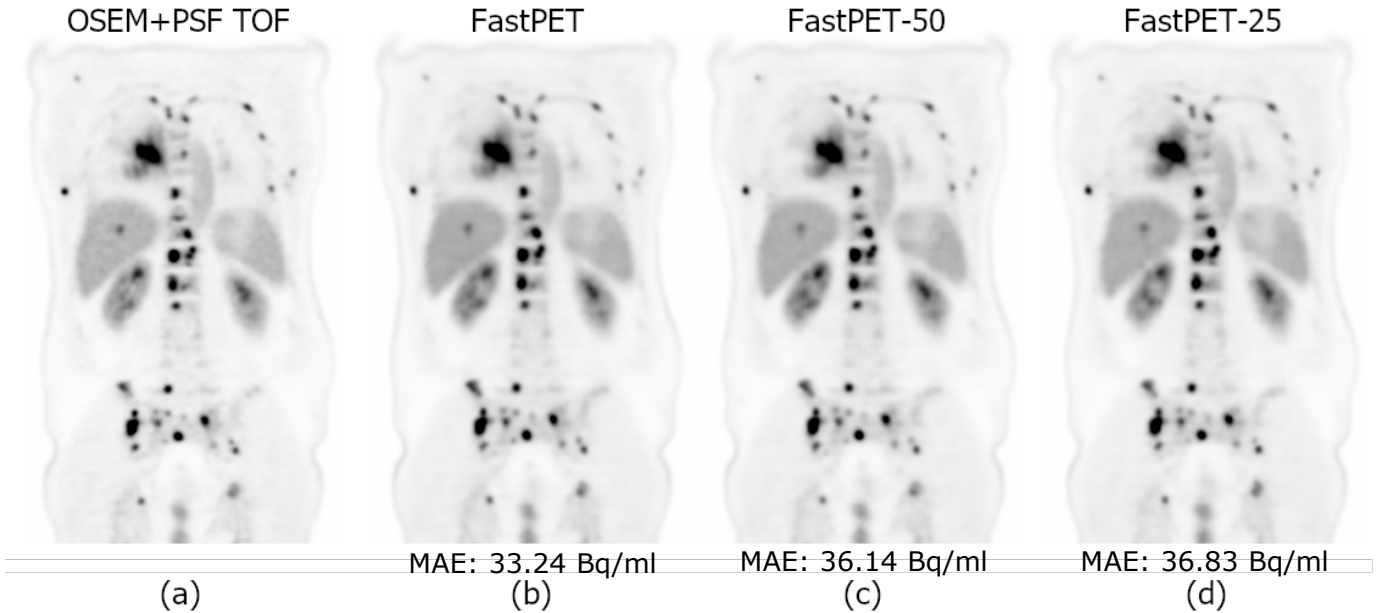


Fig. 8. A coronal view comparison between conventional OSEM+PSF TOF reconstruction and the FastPET neural network and its low count variants is shown for validation patient 7 with many varying sized lesions. The mean absolute error is also displayed below each image showing relative consistency even as the number of raw counts decreases.

of variance in all cases, including those with only 50% and 25% counts. For example FastPET-Chest, which achieved the highest performance, recovered 94.3% of the target tracer compared to an estimated 78.1% for OSEM+PSF with the same level of variance. Similar results are seen in Figure 6b for the small liver lesion where 3 out of 4 FastPET variants recover more tracer per unit variance with FastPET-25 this time falling slightly below the blue line.

A similar quantitative measure shown in Figure 7a of signal-to-noise ratio (SNR) calculated from ROIs in the liver across all 8 test patients further supports the contrast recovery measurements. In all cases the SNR for the neural network reconstructions was higher than conventional iterative reconstruction due to the reduced noise. Generally speaking, low noise images produced by neural networks are not surprising due to the way network parameters are optimized over a large data distribution through gradient descent. While the smoothness of neural network created images is not itself inherently bad, any accompanying degradation to tracer recovery or spatial resolution does negatively affect quantitative image quality and should be minimized.

Bias was also calculated across all test patients from ROIs in the liver with the results shown in Figure 7b. The FastPET neural networks appear to exhibit non-systematic random bias referenced to the OSEM+PSF TOF target with an average deviation of 4.2% and a max of 7.7%.

D. Qualitative Image Performance

In this section, a variety of image sets are explored to evaluate the qualitative performance of FastPET compared to the benchmark iterative reconstruction method of OSEM+PSF TOF. Table III shows a summary of perceptual similarity measures across the validation patient population for the histo image input, the FastPET network variants and iterative reconstruction benchmarks on the low count data. The measurements indicate that FastPET, and its variants, are perceptually very similar to the target images with an average MS-SSIM measure of 0.987 for FastPET, 0.985 for FastPET-50 and 0.982 for FastPET-25. By contrast, the low count iterative reconstructions measured 0.875 for OSEM+PSF-50 and 0.701 for OSEM+PSF-25.

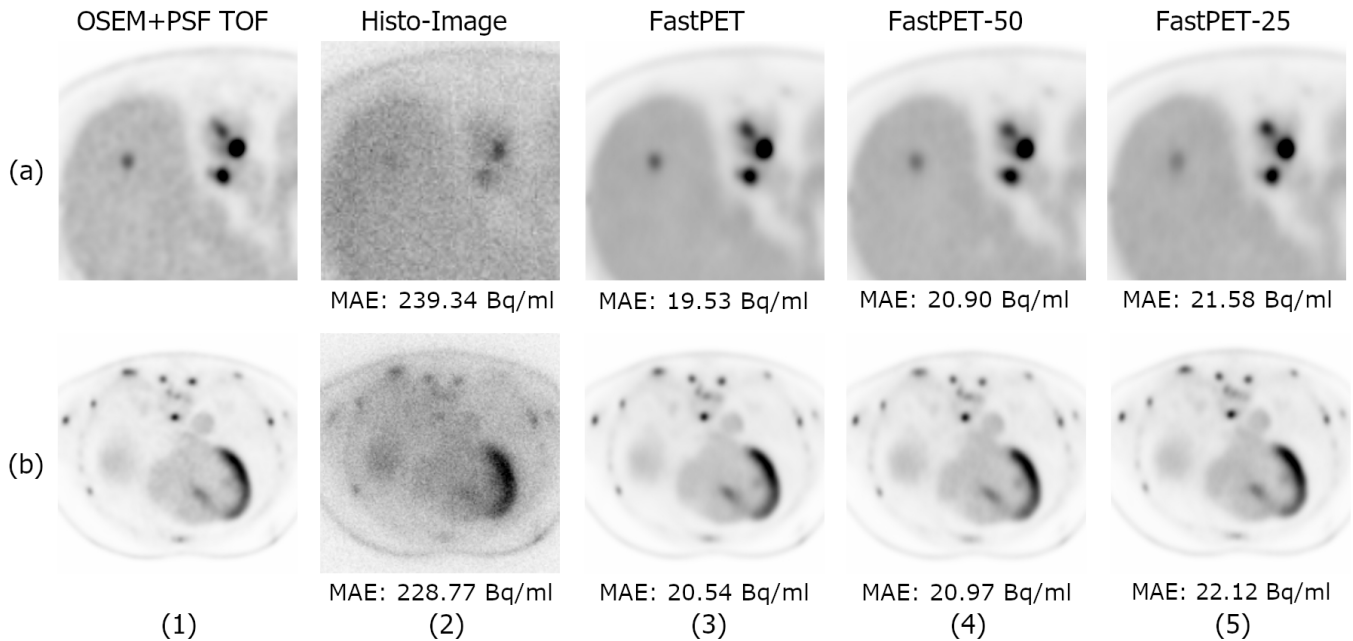


Fig. 9. Transaxial image slice comparison between the various reconstruction methods and additionally including the input histo-image for comparison. A zoomed in view of the liver and various sized lesions is shown in row (a) and a view of the heart and multiple small lesions in the bone is shown in row (b). These images clearly contrast the different noise characteristics of histo-images, conventional iterative reconstruction and neural network reconstruction methods.

In Figure 8 a coronal image of a patient with many lesions of varying sizes is reconstructed with the iterative PET benchmark, FastPET and its low count variants. Close investigation of the many lesions indicates a strong visual similarity between the images. Even the images created from lower count data seem to contain all of the lesions in the reference with some slight degradation in the lower intensity lesions for the FastPET-25 image. However, the mean absolute error is relatively consistent across the images at about 2.5% given a mean voxel value of 1410 Bq/ml. One minor artifact specifically present in a coronal view is a layering effect barely visible at the top of the liver in the FastPET image (Figure 8b). This effect is due to the neural network reconstructing 8 slice axial volumes independently from adjacent volumes and is similar to the artifacts occasionally seen on the boundaries in conventional multi-bed PET scans. This artifact will be addressed in future work potentially through additional convolutions with an axial versus transaxial orientation.

In Figure 9 transaxial images are presented for each of the reconstruction methods along with the histo-image to visualize the input to the neural network. In row (a), a zoomed image of the liver and various lesions are shown. The contrast between the noise levels of the histo-image, conventional reconstruction and the neural network outputs are clearly visible. While the intensity of the liver lesion seems to diminish slightly in FastPET-50 and FastPET-25, the more intense concentration tracer is well defined in all three neural network reconstructions. With an average voxel value 868 Bq/ml the mean absolute error across the FastPET images is about 2.4%. In row (b), a slice containing the heart with multiple small lesions in the bone tissue is presented. Again,

the contrast between the various noise levels is distinct, but despite the significantly smoother images, the neural network does recover each of the small lesions and exhibits similar perfusion in the heart muscle. In this case the mean absolute error across the FastPET realizations is 2.2% with a mean voxel value of 954 Bq/ml.

Figure 10 and 11 explore the qualitative performance of FastPET networks trained specifically on a subset of anatomy. FastPET-Brain, shown in Figure 10, was fine tuned on a neurology data set. PET neurology imaging with ^{18}F FDG is often challenging due to the relatively high uptake in brain tissue and the high density of closely spaced structures. However, on the beneficial side, brain data is less sparse and has higher magnitude than comparable PET wholebody data. Despite the potential challenges, FastPET-Brain achieved the overall lowest loss of all the neural networks during training. In this case, a low loss seemed to translate to high qualitative image quality. The brain images in Figure 10b are nearly indistinguishable from the FastPET-Brain images in the row below with a average mean absolute error across the four validation patients of only 0.98% with a mean voxel value of 1403 Bq/ml.

FastPET-Chest is another example of an anatomically focused neural network that, in this case, was fine tuned through training specifically on the chest region of PET wholebody scans. The chest region in particular can have widely varying distributions and intensities of tracer concentration from high intensity in the heart and lesions to virtually no tracer in the lungs. A sampling of chest images is shown in Figure 11 including the histo-image, iterative reconstruction and FastPET-Chest reconstruction. The distinct contrast in noise levels is

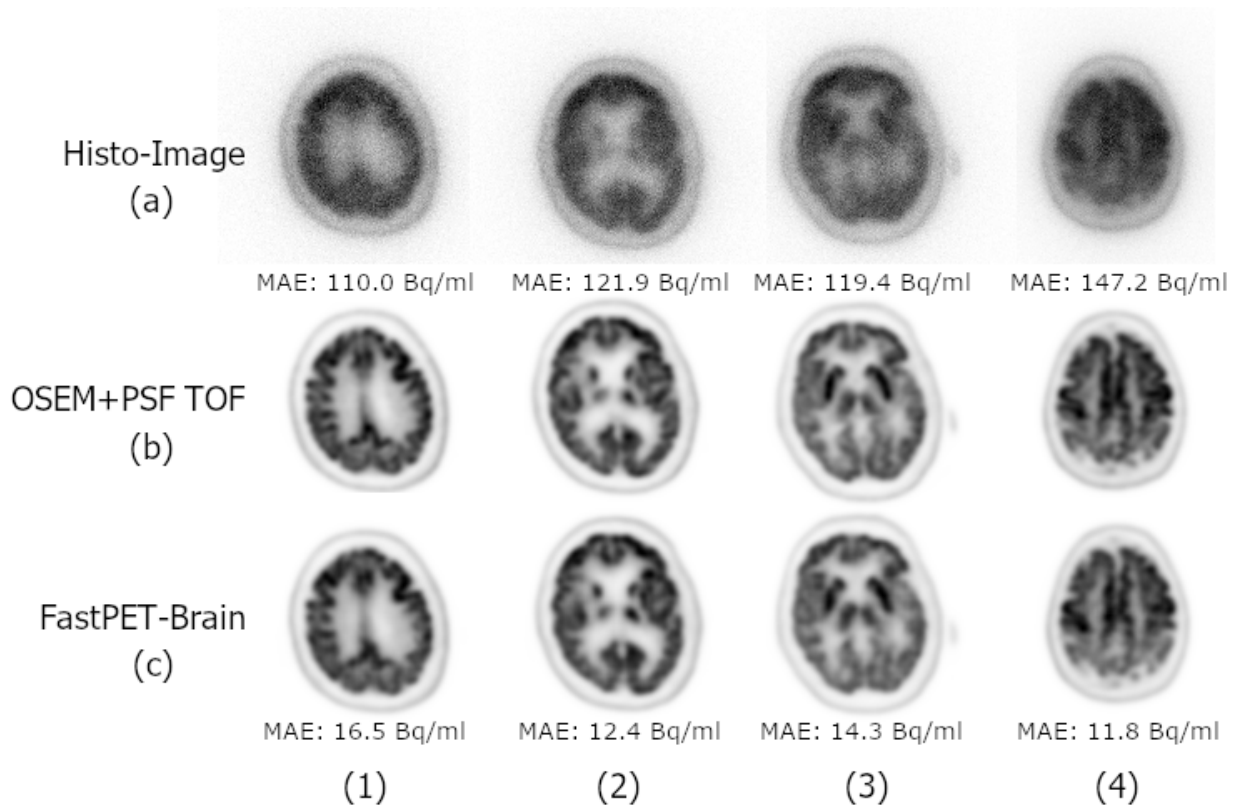


Fig. 10. Transaxial image slices comparison from neurology studies comparing the histo-image input, conventional reconstruction and FastPET-Brain reconstruction, which is a neural network variant specifically fine tuned on a neurology data set.

evident with the neural network producing smooth images, but also preserving the anatomical structures. The average mean absolute error over the three cases shown is 1.8% with an mean voxel value of 897 Bq/ml, which out performs the wholebody FastPET variants but does not achieve the performance of the brain focused network.

V. DISCUSSION AND CHALLENGES

The FastPET experiments clearly and consistently produce visually smooth images with structural components nearly identical to conventional OSEM+PSF TOF reconstructions. Generally speaking, absence of high frequency details could mean the removal of small lesions or other critical details. While this concern was not clearly evident in our limited population of 8 test patients, the quantitative measurements of FastPET in our experiments demonstrated room for improvement in the area of contrast recovery and random bias reduction compared to conventional iterative reconstruction.

Future work on quantitative performance improvement will focus on better loss functions and tuning of the target data set. Loss functions that reward preservation of high frequency details while balancing the noise content will be explored. Regarding data set tuning, in this initial FastPET work, 3 iterations of OSEM+PSF TOF were utilized to create the target images because it was the factory default and constitutes a reasonable balance between variance and bias. However, given FastPET's propensity to produce smooth images, it might be

beneficial, from a contrast recovery aspect, to create higher variance target images using a higher number of iterations. Alternatively, the exploration of including simulated training targets where the variance could be precisely controlled may lead to additional insights on improving quantitative performance.

The fine tuning of neural networks in this work using transfer learning for specific tasks in the areas of low dose PET imaging and networks with an anatomical focus provided interesting results. In the low dose case, both FastPET variants were able to produce quality images with much fewer counts with FastPET-50 performing nearly identical to the baseline FastPET across the patients in the test set, and FastPET-25 degrading slightly in comparison and hinting at a lower limit to low dose imaging with the proposed method. In the area of anatomical focus, the fine tuned networks showed improvements both in the quantitative domain in the case of FastPET-Chest having the highest contrast recovery and the lowest average absolute bias, and in the qualitative domain where FastPET-Brain produced nearly identical brain images and achieved the lowest loss for both absolute and perceptual measures. These results of networks focused on a specific subset of data perhaps points to a path of overall improvement where a multitude of neural networks are trained and a particular type of PET data is funneled to the most appropriate neural network.

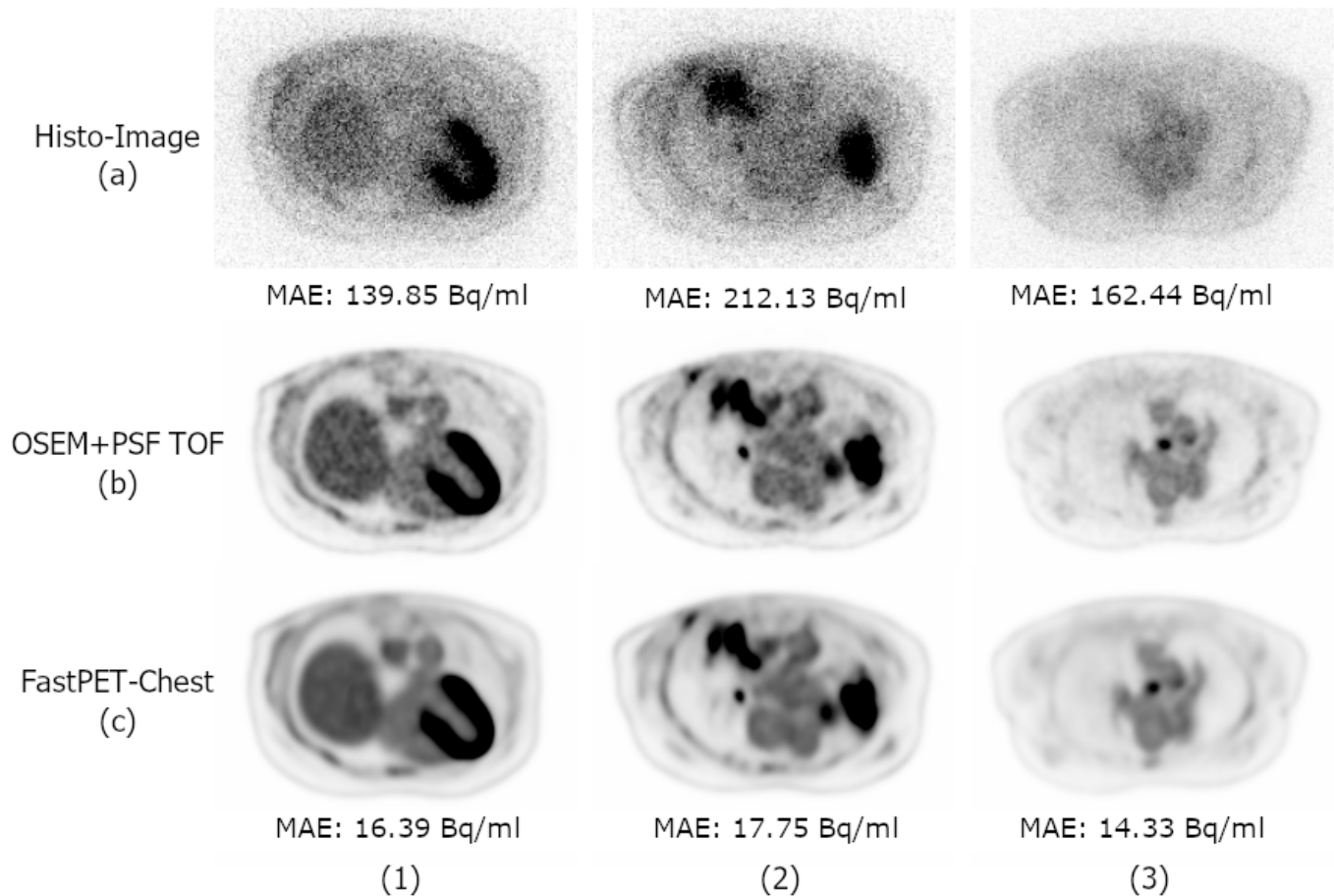


Fig. 11. Transaxial chest images are presented comparing the histo-image input, conventional iterative reconstruction and FastPET-Chest reconstruction. In a similar fashion to the other figures, the distinctly low noise characteristics is evident in the neural network reconstructions.

VI. CONCLUSION

The FastPET reconstruction method proposed in this work is capable of full size multi-slice reconstruction of PET data from histo-images in near real-time. This simple architecture consists of a most likely annihilation position histogrammer and a convolutional neural network. Raw PET data is processed by the histogrammer and the resulting histo-images along with the corresponding attenuation maps are fed to the neural network to produce the final PET images. Experiments measured the quantitative and qualitative aspects of FastPET image quality compared to a conventional time-of-flight iterative reconstruction methods. The results showed the proposed method produced high quality images with low noise, but could be improved in the areas of contrast recovery and bias reduction. Beyond the basic FastPET network, additional task specific neural networks were trained in the areas of low dose PET imaging and anatomically focused imaging using the process of transfer learning. In both cases, the task specific FastPET versions showed improvements over the original version.

ACKNOWLEDGMENT

The authors would like to thank Paul Luk for providing valuable support and feedback throughout the development of FastPET.

REFERENCES

- [1] H. M. Hudson and R. S. Larkin, "Accelerated image reconstruction using ordered subsets of projection data," *IEEE Transactions on Medical Imaging*, vol. 13, no. 4, pp. 601–609, Dec 1994.
- [2] V. Y. Panin, F. Kehren, C. Michel, and M. Casey, "Fully 3-d pet reconstruction with system matrix derived from point source measurements," *IEEE Transactions on Medical Imaging*, vol. 25, no. 7, pp. 907–921, July 2006.
- [3] S. Matej, S. Jayanthi, S. Surti, M. E. Daube-Witherspoon, G. Muehllehner, and J. S. Karp, "Efficient 3D TOF PET reconstruction using view-grouped histo-images: DIRECT - direct image reconstruction for TOF," in *2006 IEEE Nuclear Science Symposium Conference Record*, vol. 3, Oct 2006, pp. 1728–1735.
- [4] S. Vandenberghe, M. E. Daube-Witherspoon, R. M. Lewitt, and J. S. Karp, "Fast reconstruction of 3d time-of-flight PET data by axial rebinning and transverse mashing," *Physics in Medicine and Biology*, vol. 51, no. 6, pp. 1603–1621, mar 2006. [Online]. Available: <https://doi.org/10.1088%2F0031-9155%2F51%2F6%2F017>
- [5] D. L. Snyder, L. J. Thomas, and M. M. Ter-Pogossian, "A mathematical model for positron-emission tomography systems having time-of-flight measurements," *IEEE Transactions on Nuclear Science*, vol. 28, no. 3, pp. 3575–3583, June 1981.
- [6] D. G. Politte, G. R. Hoffman, D. E. Beecher, D. C. Ficke, T. J. Holmes, and M. M. Ter-Pogossian, "Image-reconstruction of data from super pett i: A first-generation time-of-flight positron-emission tomograph," *IEEE Transactions on Nuclear Science*, vol. 33, no. 1, pp. 428–434, Feb 1986.
- [7] N. Mullani, W. Wong, P. Hartz, E. Philippe, and K. Yerian, "Sensitivity improvement of totpet by the utilization of the inter-slice coincidences," *Nuclear Science, IEEE Transactions on*, vol. 29, pp. 479 – 483, 03 1982.
- [8] Silin Ren, X. Jin, C. Chan, Yiqiang Jian, T. Mulnix, Chi Liu, and R. E. Carson, "Data-driven respiratory motion estimation and correction using tof pet list-mode centroid of distribution," in *2014 IEEE Nuclear Science*

- Symposium and Medical Imaging Conference (NSS/MIC)*, Nov 2014, pp. 1–5.
- [9] V. Y. Panin and H. Bal, “Tof data non-rigid motion correction,” in *2015 IEEE Nuclear Science Symposium and Medical Imaging Conference (NSS/MIC)*, Oct 2015, pp. 1–5.
- [10] V. Jain and H. S. Seung, “Natural image denoising with convolutional networks,” in *Proceedings of the 21st International Conference on Neural Information Processing Systems*, ser. NIPS08. Red Hook, NY, USA: Curran Associates Inc., 2008, p. 769776.
- [11] J. Xie, L. Xu, and E. Chen, “Image denoising and inpainting with deep neural networks,” *Advances in Neural Information Processing Systems*, vol. 1, 01 2012.
- [12] K. Zhang, W. Zuo, Y. Chen, D. Meng, and L. Zhang, “Beyond a gaussian denoiser: Residual learning of deep CNN for image denoising,” *IEEE Transactions on Image Processing*, vol. 26, no. 7, pp. 3142–3155, July 2017.
- [13] C. Tian, Y. Xu, L. Fei, and K. Yan, “Deep learning for image denoising: A survey,” in *Genetic and Evolutionary Computing*, J.-S. Pan, J. C.-W. Lin, B. Sui, and S.-P. Tseng, Eds. Singapore: Springer Singapore, 2019, pp. 563–572.
- [14] W. Yang, H. Zhang, J. Yang, J. Wu, X. Yin, Y. Chen, H. Shu, L. Luo, G. Coatrieux, Z. Gui, and Q. Feng, “Improving low-dose CT image using residual convolutional network,” *IEEE Access*, vol. 5, pp. 24 698–24 705, 2017.
- [15] E. Kang, W. Chang, J. Yoo, and J. C. Ye, “Deep convolutional framelet denoising for low-dose CT via wavelet residual network,” *IEEE Transactions on Medical Imaging*, vol. 37, no. 6, pp. 1358–1369, June 2018.
- [16] M. Gholizadeh-Ansari, J. Alirezaie, and P. Babyn, “Low-dose ct denoising with dilated residual network,” in *2018 40th Annual International Conference of the IEEE Engineering in Medicine and Biology Society (EMBC)*, July 2018, pp. 5117–5120.
- [17] Y. Han and J. C. Ye, “Framing U-Net via deep convolutional framelets: Application to sparse-view CT,” *IEEE Transactions on Medical Imaging*, vol. 37, no. 6, pp. 1418–1429, June 2018.
- [18] D. Jiang, W. Dou, L. P. J. Vosters, X. Xu, Y. Sun, and T. Tan, “Denoising of 3D magnetic resonance images with multi-channel residual learning of convolutional neural network,” *Japanese Journal of Radiology*, vol. 36, pp. 566–574, 2017.
- [19] Y. Wang, Y. Song, H. Xie, W. Li, B. Hu, and G. Yang, “Reduction of gibbs artifacts in magnetic resonance imaging based on convolutional neural network,” in *2017 10th International Congress on Image and Signal Processing, BioMedical Engineering and Informatics (CISP-BMEI)*, Oct 2017, pp. 1–5.
- [20] J. Xu, E. Gong, J. Pauly, and G. Zaharchuk, “200x Low-dose PET Reconstruction using Deep Learning,” *arXiv e-prints*, p. arXiv:1712.04119, Dec 2017.
- [21] K. Gong, J. Guan, C. Liu, and J. Qi, “PET image denoising using a deep neural network through fine tuning,” *IEEE Transactions on Radiation and Plasma Medical Sciences*, vol. 3, no. 2, pp. 153–161, March 2019.
- [22] S. J. Kaplan and Y.-M. Zhu, “Full-dose PET image estimation from low-dose PET image using deep learning: a pilot study,” *Journal of Digital Imaging*, vol. 32, no. 5, pp. 773–778, October 2018.
- [23] W. Lu, J. A. Onofrey, Y. Lu, L. Shi, T. Ma, Y. Liu, and C. Liu, “An investigation of quantitative accuracy for deep learning based denoising in oncological PET,” *Physics in Medicine & Biology*, vol. 64, no. 16, p. 165019, aug 2019. [Online]. Available: <https://doi.org/10.1088%2F1361-6560%2F64%2F16%2F165019>
- [24] O. Ronneberger, P. Fischer, and T. Brox, “U-net: Convolutional networks for biomedical image segmentation,” in *Medical Image Computing and Computer-Assisted Intervention (MICCAI)*, ser. LNCS, vol. 9351. Springer, 2015, pp. 234–241, (available on arXiv:1505.04597 [cs.CV]). [Online]. Available: <http://lmb.informatik.uni-freiburg.de/Publications/2015/RFB15a>
- [25] K. He, X. Zhang, S. Ren, and J. Sun, “Deep residual learning for image recognition,” in *2016 IEEE Conference on Computer Vision and Pattern Recognition (CVPR)*, June 2016, pp. 770–778.
- [26] J. Jiao and S. Ourselin, “Fast PET reconstruction using Multi-scale Fully Convolutional Neural Networks,” *arXiv e-prints*, p. arXiv:1704.07244, Apr 2017.
- [27] C. E. Floyd, J. E. Bowsher, M. T. Munley, G. D. Tourassi, S. Garg, A. H. Baydush, J. Y. Lo, and R. E. Coleman, “Artificial neural networks for SPECT image reconstruction with optimized weighted backprojection,” in *Conference Record of the 1991 IEEE Nuclear Science Symposium and Medical Imaging Conference*, Nov 1991, pp. 2184–2188 vol.3.
- [28] A. Bevilacqua, D. Bollini, R. Campanini, N. Lanconelli, M. Galli, and V. Don Fiammelli, “A new approach to Positron Emission Tomography (PET) image reconstruction using Artificial Neural Networks (ANN),” *International Journal of Modern Physics C*, vol. 9, 11 2000.
- [29] P. Paschalidis, N. D. Giokaris, A. Karabarounis, G. K. Loudos, D. Maintas, C. N. Papanicolas, V. Spanoudaki, C. Tsoumpas, and E. Stiliaris, “Tomographic image reconstruction using Artificial Neural Networks,” *Nuclear Instruments and Methods in Physics Research A*, vol. 527, pp. 211–215, Jul. 2004.
- [30] M. Argyrou, D. Maintas, C. Tsoumpas, and E. Stiliaris, “Tomographic image reconstruction based on artificial neural network (ANN) techniques,” in *2012 IEEE Nuclear Science Symposium and Medical Imaging Conference Record (NSS/MIC)*, Oct 2012, pp. 3324–3327.
- [31] G. Wang, J. C. Ye, K. Mueller, and J. A. Fessler, “Image reconstruction is a new frontier of machine learning,” *IEEE Transactions on Medical Imaging*, vol. 37, no. 6, pp. 1289–1296, June 2018.
- [32] A. Paszke, S. Gross, S. Chintala, G. Chanan, E. Yang, Z. DeVito, Z. Lin, A. Desmaison, L. Antiga, and A. Lerer, “Automatic differentiation in PyTorch,” in *NIPS-W*, 2017.
- [33] M. Abadi, A. Agarwal, P. Barham, E. Brevdo, Z. Chen, C. Citro, G. S. Corrado, A. Davis, J. Dean, M. Devin, S. Ghemawat, I. Goodfellow, A. Harp, G. Irving, M. Isard, Y. Jia, R. Jozefowicz, L. Kaiser, M. Kudlur, J. Levenberg, D. Mané, R. Monga, S. Moore, D. Murray, C. Olah, M. Schuster, J. Shlens, B. Steiner, I. Sutskever, K. Talwar, P. Tucker, V. Vanhoucke, V. Vasudevan, F. Viégas, O. Vinyals, P. Warden, M. Wattenberg, M. Wicke, Y. Yu, and X. Zheng, “TensorFlow: Large-scale machine learning on heterogeneous systems,” 2015, software available from tensorflow.org. [Online]. Available: <https://www.tensorflow.org/>
- [34] B. Zhu, J. Z. Liu, B. R. Rosen, and M. S. Rosen, “Image reconstruction by domain-transform manifold learning,” *Nature*, vol. 555, pp. 487–492, 2018.
- [35] W. Whiteley and J. Gregor, “Efficient neural network image reconstruction from raw data using a radon inversion layer,” in *2019 IEEE Nuclear Science Symposium and Medical Imaging Conference (NSS/MIC)*, Nov 2019, pp. 1–2.
- [36] I. Heggström, C. R. Schmidlein, G. Campanella, and T. J. Fuchs, “DeepPET: A deep encoder-decoder network for directly solving the PET image reconstruction inverse problem,” *Medical Image Analysis*, vol. 54, pp. 253 – 262, 2019. [Online]. Available: <http://www.sciencedirect.com/science/article/pii/S1361841518305838>
- [37] K. He, X. Zhang, S. Ren, and J. Sun, “Delving deep into rectifiers: Surpassing human-level performance on imagenet classification,” in *Proceedings of the 2015 IEEE International Conference on Computer Vision (ICCV)*, ser. ICCV 15. USA: IEEE Computer Society, 2015, p. 10261034. [Online]. Available: <https://doi.org/10.1109/ICCV.2015.123>
- [38] W. Shi, J. Caballero, F. Huszár, J. Totz, A. P. Aitken, R. Bishop, D. Rueckert, and Z. Wang, “Real-time single image and video super-resolution using an efficient sub-pixel convolutional neural network,” *2016 IEEE Conference on Computer Vision and Pattern Recognition (CVPR)*, pp. 1874–1883, June 2016.
- [39] D. P. Kingma and J. Ba, “Adam: A method for stochastic optimization,” *International Conference on Learning Representations ICLR('14)*, 2014.
- [40] L. N. Smith, “Cyclical learning rates for training neural networks,” *2017 IEEE Winter Conference on Applications of Computer Vision (WACV)*, pp. 464–472, 2015.
- [41] H. Zhao, O. Gallo, I. Frosio, and J. Kautz, “Loss functions for image restoration with neural networks,” *IEEE Transactions on Computational Imaging*, vol. 3, no. 1, pp. 47–57, March 2017.
- [42] Z. Wang, A. C. Bovik, H. R. Sheikh, and E. P. Simoncelli, “Image quality assessment: from error visibility to structural similarity,” *IEEE Transactions on Image Processing*, vol. 13, no. 4, pp. 600–612, April 2004.
- [43] K. Simonyan and A. Zisserman, “Very Deep Convolutional Networks for Large-Scale Image Recognition,” *arXiv e-prints*, p. arXiv:1409.1556, Sep 2014.
- [44] J. J. van Sluis, J. d. Jong, J. Schaar, W. Noordzij, P. v. Snick, R. Dierckx, R. Borra, A. Willemsen, and R. Boellaard, “Performance characteristics of the digital biograph vision PET/CT system,” *Journal of Nuclear Medicine*, vol. 60, pp. 1031–1036, July 2019.

William Whiteley is a Director of software engineering at Siemens Medical Solutions USA, Inc. working in molecular imaging and a PhD student at The University of Tennessee, Knoxville studying artificial intelligence and image reconstruction. He received his BSEE degree from Vanderbilt University, Nashville, TN and his MSEE degree from Stanford University, Stanford, CA. His research interests include artificial intelligence, deep learning, medical imaging, and data mining.

Dr. Vladimir Panin is a Senior Key Expert at Siemens Medical Solutions USA, Inc. He received his Diploma in Theoretical Physics from Moscow Engineering Physics Institute and PhD from Physics Department, University of Utah. His research interests include PET/CT image reconstruction and data corrections.

Dr. Chuanyu Zhou is a staff software engineer at Siemens Medical Solutions USA, Inc. He received his PhD degree from the department of Aerospace Engineering and MS degree from department of Electrical and Computer Engineering department, Iowa State University. His research interests include PET/CT image reconstruction, image processing, deep learning and high performance computing.

Dr. Jorge Cabello is a research scientist in the Physics and Reconstruction group at Siemens Medical Solutions USA, Inc. He received his PhD from Surrey University, UK, and his MSEE and BSEE degrees from Universidad de Alcalá, Spain. His research interests cover image reconstruction, Monte Carlo simulations, artificial intelligence and detector physics.

Dr. Deepak K Bharkhada is a staff Scientist in the molecular imaging division of Siemens Medical Solutions USA, Inc. He has a PhD in Biomedical Engineering from a joint program between Wake Forest University and Virginia Polytechnic, MS from Drexel University, and BE from Mumbai University. His research interests include image reconstruction and corrections for tomographic imaging modalities like PET and CT and artificial intelligence.

Dr. Jens Gregor received his PhD in Electrical Engineering from Aalborg University Denmark, in 1991. He then joined the faculty at the University of Tennessee, Knoxville, where he currently holds the position of Professor and Associate Department Head in the Department of Electrical Engineering and Computer Science. His research has covered different imaging modalities including X-ray and neutron CT, SPECT, and PET with applications ranging from industrial and security imaging to preclinical and clinical imaging.